



# Dual role of sulfur doping in NiCr LDH for water oxidation: Promoting surface reconfiguration and lattice oxygen oxidation

Qiaohong Su<sup>a</sup>, Pengyue Wang<sup>a</sup>, Qingcui Liu<sup>a</sup>, Rui Sheng<sup>a</sup>, Wenhua Cheng<sup>a</sup>, Juan Ding<sup>a</sup>,  
Yongpeng Lei<sup>b,\*</sup>, Yudai Huang<sup>a,\*</sup>

<sup>a</sup> State Key Laboratory of Chemistry and Utilization of Carbon Based Energy Resources; College of Chemistry, Xinjiang University, Urumqi, 830017, Xinjiang, P. R. China

<sup>b</sup> State Key Laboratory of Powder Metallurgy, Central South University, Changsha, 410083, Hunan, P. R. China

## ARTICLE INFO

### Keywords:

Doping  
NiCr LDH  
Surface reconfiguration  
Cr leaching  
Lattice oxygen oxidation

## ABSTRACT

Heterogeneous doping is widely applied to improve the oxygen evolution reaction (OER) activity of layered double metal hydroxides (LDH), but it is challenging to study the reconfiguration and reaction mechanism of catalysts. Herein, we prepared sulfur-doped NiCr LDH (S<sub>x</sub>-NiCr LDH) pre-catalyst, which exhibits low overpotential of 244.4 mV at 100 mA cm<sup>-2</sup> after reconfiguration. The characterization results reveal that sulfur doping not only optimizes the reconfiguration process of NiCr LDH by modulating Cr leaching, but also reduces the oxidation potential of Ni<sup>2+</sup>. Density functional theory (DFT) results show that sulfur doping reduces the energy barrier of reconfiguration, enhances the covalency of Ni-O, and upshifts the O 2p band center to promote lattice oxygen oxidation. The reconfigured catalyst requires 1.51 and 1.47 V at 10 mA cm<sup>-2</sup> for overall water splitting at 25 °C and 80 °C, respectively. This work provides a valuable approach for designing highly active LDH catalysts.

## 1. Introduction

The oxygen evolution reaction (OER) is the key step that limits the efficiency of water electrolysis [1–3]. Two key factors that determine OER catalyst activity include reaction mechanism and active phase. Currently, conventional adsorption evolution mechanism (AEM) and lattice oxygen mechanism (LOM) are adapted to reveal the alkaline OER mechanism [4,5]. AEM is limited by the scaling relationships of the adsorption energy difference between the \*OH and \*OOH intermediates ( $\Delta G^{\circ}_{\text{OOH}} - \Delta G^{\circ}_{\text{OH}} = 3.2$  eV), leading to a minimum theoretical overpotential of 0.37 V to trigger the OER reaction [6,7]. LOM involves the direct formation of O-O through coupling between lattice oxygen and \*O, which can bypass this limitation in AEM [8,9]. To trigger the LOM, the O 2p band needs to be upshifted close to the Fermi level ( $E_F$ ), which enhances its orbital overlap with the metal d-band (M-O covalent bond), and makes lattice oxygen oxidation more favorable [10,11]. Many excellent works have reported heteroatom doping strategies to activate lattice oxygen. For example, Liu et al. [12] reported Zn, S co-doped Fe<sub>2</sub>O<sub>3</sub>/Fe<sub>3</sub>O<sub>4</sub>/IF pre-catalysts, where sulfur leaching promotes the reconfiguration of Zn, S-Fe<sub>2</sub>O<sub>3</sub> into Zn-FeOOH, and the formation of Zn-FeOOH raises the O 2p bands and activates lattice oxygen. Wang

et al. [13] reported Ir single-atom loading on reconfigured Ni-doped CoOOH, where the Co site undergoes AEM path and the lattice O bridging the Ni and Ir atoms is activated by coupling with adsorbed O on the Ir site. Therefore, modulating the OER mechanism by heteroatom doping provides another feasible way to design catalysts with high OER activity.

Usually, catalyst is reconfigured into active metal oxyhydroxides (MOOH, M stands for metal) during the OER process [14,15]. Some studies have reported that heteroatoms (F, Mo, Zn and Cr) are doped into the host material and then the dopants are leaching through electrochemical activation to induce self-reconfiguration of the catalyst [16–19]. For example, Malek et al. [19] reported that Cr leaching induced dynamic reconfiguration of the Ni<sub>x</sub>Cr<sub>y</sub>O catalyst during the OER process, which increased the porosity and electrochemically active area. Duan et al. [20] reported that CoCr<sub>2</sub>O<sub>4</sub> is prepared by replacing Co in Co<sub>3</sub>O<sub>4</sub> with Cr, and then regulated Cr leaching by activating CoCr<sub>2</sub>O<sub>4</sub> at high potential to promote reconfiguration into active CoOOH. Moreover, the surface reconstruction induced by Cr leaching during the OER process involves the depletion of lattice oxygen, thus triggering LOM. However, efforts aimed at modulating ion leaching to promote self-reconfiguration and optimize LOM path through heteroatom doping

\* Corresponding authors.

E-mail addresses: [leiyongpeng@csu.edu.cn](mailto:leiyongpeng@csu.edu.cn) (Y. Lei), [huangyd@xju.edu.cn](mailto:huangyd@xju.edu.cn) (Y. Huang).

<https://doi.org/10.1016/j.apcatb.2024.123994>

Received 22 January 2024; Received in revised form 7 March 2024; Accepted 20 March 2024

Available online 21 March 2024

0926-3373/© 2024 Elsevier B.V. All rights reserved.

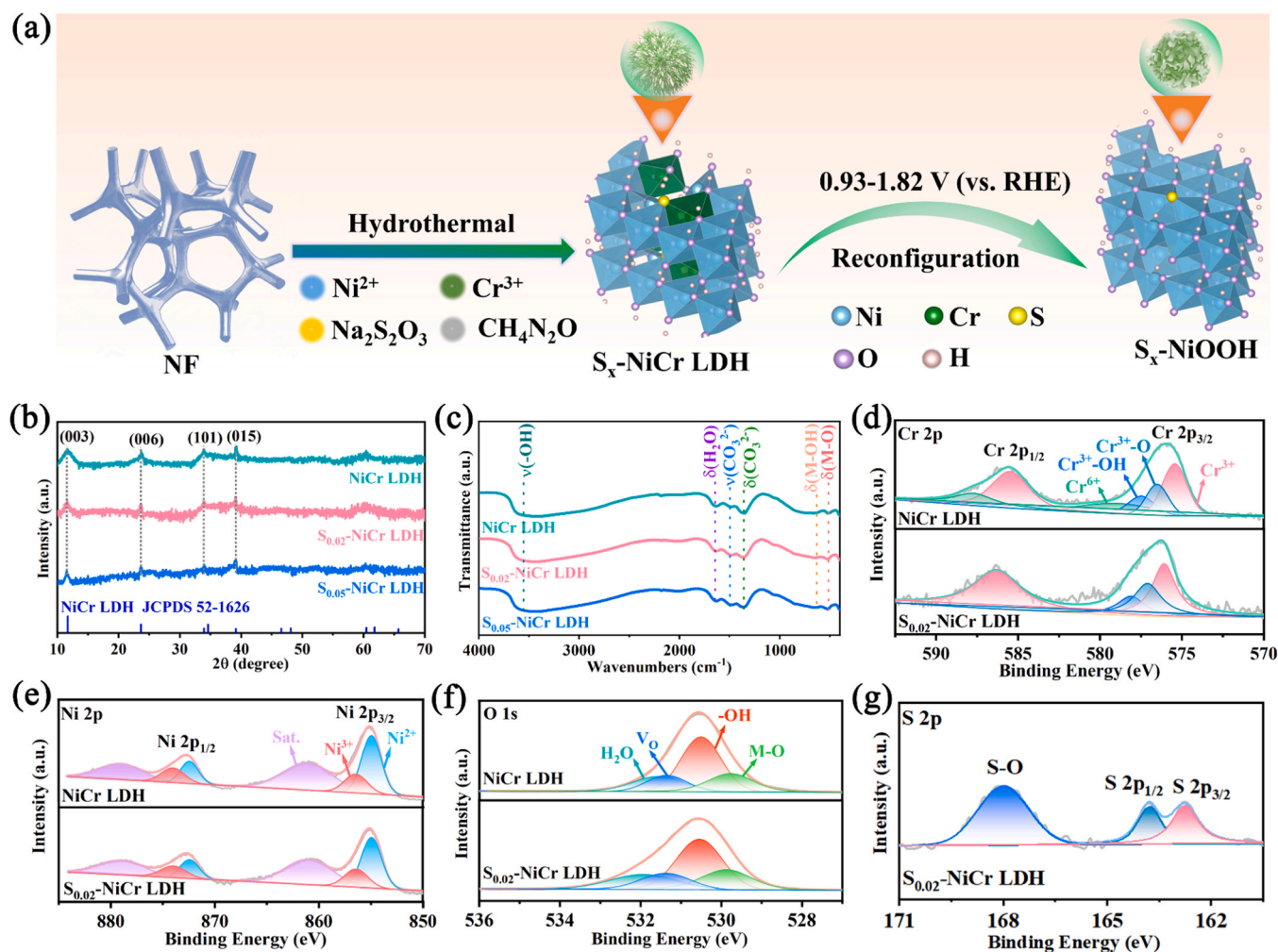


**Fig. 1.** (a) Schematic diagram of catalyst preparation. (b) XRD patterns and (c) FTIR spectra of NiCr LDH,  $S_{0.02}$ -NiCr LDH, and  $S_{0.05}$ -NiCr LDH. XPS spectra of NiCr LDH and  $S_{0.02}$ -NiCr LDH: (d) Cr 2p, (e) Ni 2p, and (f) O 1s. (g) S 2p XPS spectrum of  $S_{0.02}$ -NiCr LDH.

strategies are still limited.

In this work, we report sulfur-doped nickel-chromium layered double hydroxide ( $S_x$ -NiCr LDH) as pre-catalysts, and then activate it at high potential to promote reconfiguration. The reconfigured catalyst has a low overpotential of 244.4 mV at 100 mA cm<sup>-2</sup>. Furthermore, it requires a voltage of 1.51 and 1.47 V at 10 mA cm<sup>-2</sup> for overall water splitting at 25 °C and 80 °C, respectively. The role of sulfur doping on the surface reconfiguration and reaction mechanism of catalysts is revealed by diverse characterization and density functional theory (DFT). The results show that sulfur doping not only lowers the reconfiguration energy barrier and promotes the reconfiguration process, but also effectively elevates the covalency of Ni-O and upshifts the O 2p band center, thereby promoting lattice oxygen oxidation.

## 2. Results and discussion

### 2.1. Structural characterization of pre-catalysts

NiCr LDH and sulfur doped NiCr LDH ( $S_x$ -NiCr LDH, with  $x$  representing the molar ratio of  $Na_2S_2O_3$  to the total metal) were prepared as pre-catalysts, and then activated at potentials ranging from 0.93 to 1.82 V versus the reversible hydrogen electrode (vs. RHE) (Fig. 1a). Scanning electron microscopy (SEM) images show that the NiCr LDH exhibits a typical nanosheet morphology, whereas  $S_{0.02}$ -NiCr LDH shows a network morphology (Fig. S1a, b). With further increase the sulfur content,  $S_{0.05}$ -NiCr LDH evolves into small nanosheets (Fig. S1c). The

results indicate that sulfur doping has a great influence on the morphology of the samples. The change of the morphology was further verified by transmission electron microscopy (TEM) and high-resolution TEM (HRTEM).  $S_{0.02}$ -NiCr LDH exhibits network morphology (Fig. S2a), further corroborating the SEM results. The regions marked by yellow and green correspond to the (018) and (015) crystal faces of NiCr LDH, respectively (Fig. S2b). The elemental mapping images in Fig. S3 show that the S, O, Ni, and Cr elements are uniformly distributed on the  $S_{0.02}$ -NiCr LDH. In addition,  $S_{0.05}$ -NiCr LDH shows nanosheet morphology and has the same crystal faces as  $S_{0.02}$ -NiCr LDH (Fig. S2c, d). The elemental mapping images of  $S_{0.05}$ -NiCr LDH show uniform distribution of S, O, Ni, and Cr elements on the nanosheets (Fig. S4). TEM results indicate that sulfur doping changes the morphology of the samples. The (003) and (006) peaks in the powder X-ray diffraction (XRD) patterns of  $S_{0.02}$ -NiCr LDH and  $S_{0.05}$ -NiCr LDH are attributed to the interlayer  $CO_3^{2-}$  anion, which is not shifted after sulfur doping (Fig. 1b) [21]. Moreover, the stretching vibration of interlayer  $CO_3^{2-}$  is unchanged in the fourier transform infrared (FTIR) spectra, suggests that the sulfur species is not inset into the interlayer of NiCr LDH (Fig. 1c) [22]. X-ray photoelectron spectroscopy (XPS) was performed to detect the effect of sulfur doping on the valence states of the elements. The element content is obtained from XPS, as shown in Table S1. The Cr 2p spectra of NiCr LDH split into Cr<sup>3+</sup> (575.4/585.5 eV), Cr<sup>6+</sup> (578.8/587.8 eV), Cr<sup>3+</sup>-O (576.5 eV) and Cr<sup>3+</sup>-OH (577.5 eV), indicating that the Cr species are in +3 and +6 oxidation state [23,24]. After sulfur doping, the absence of Cr<sup>6+</sup> in the Cr 2p spectra of  $S_{0.02}$ -NiCr LDH, which is due to the reduction of Cr<sup>6+</sup> by

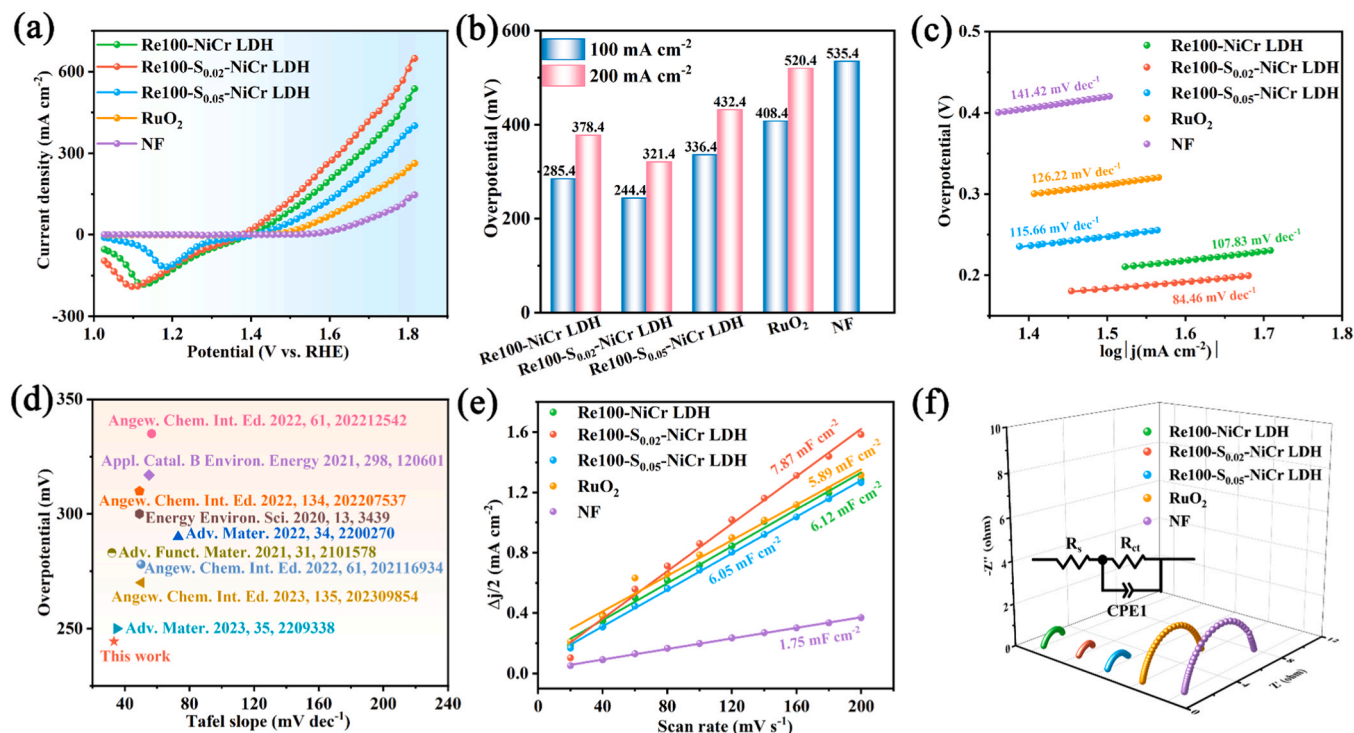


**Fig. 2.** OER performance of Re100-NiCr LDH, Re100-S<sub>0.02</sub>-NiCr LDH, Re100-S<sub>0.05</sub>-NiCr LDH, RuO<sub>2</sub>, and NF after 100 CV cycles: (a) LSV curves, (b) overpotentials at 100 and 200 mA cm<sup>-2</sup>, (c) Tafel plots, and (d) comparison of Tafel slope and overpotential for Re100-S<sub>0.02</sub>-NiCr LDH and those of previously reported literatures. (e) The capacitive currents against scan rate. (f) Nyquist plots.

Na<sub>2</sub>S<sub>2</sub>O<sub>3</sub>. Moreover, the Cr 2p peak of S<sub>0.02</sub>-NiCr LDH shifts toward the high binding energy by 0.2 eV, indicating that the electron cloud density of Cr decreases after sulfur doping (Fig. 1d). The Ni 2p spectra of NiCr LDH split into Ni<sup>2+</sup> (855.3/872.9 eV), Ni<sup>3+</sup> (856.9/874.4 eV) and satellite peaks (861.6/879.6 eV) (Fig. 1e) [25,26]. The Ni 2p peak of S<sub>0.02</sub>-NiCr LDH without obvious shift after sulfur doping. The peaks at 529.8, 530.7, 531.4 and 531.7 eV in the O 1s spectra are ascribed to lattice oxygen (M-O), hydroxyl (-OH), oxygen vacancies (V<sub>O</sub>), and adsorbed water (Fig. 1f) [27]. The peaks of S 2p<sub>1/2</sub> (163.7 eV) and S 2p<sub>3/2</sub> (162.8 eV) in the S 2p spectra belong to metal-sulfur bonds. The existence of the S-O peak (168.0 eV) is ascribed to the oxidation of surface sulfur during the preparation process (Fig. 1g) [28]. Therefore, it can be inferred from the above characterization results that the sulfur is doped as a substitute for oxygen rather than inset into the interlayers (see density functional theory (DFT) calculation model).

## 2.2. Reconfiguration of catalysts

The pre-catalysts activated by different cyclic voltammetry (CV) cycles are labeled as ReC-NiCr LDH, ReC-S<sub>0.02</sub>-NiCr LDH and ReC-S<sub>0.05</sub>-NiCr LDH (C represents the cycle number), respectively. The reconfiguration behavior was achieved by first performing 100 CV cycles in 1 M KOH solution. The CV curves of Re100-NiCr LDH, Re100-S<sub>0.02</sub>-NiCr LDH and Re100-S<sub>0.05</sub>-NiCr LDH show that with the gradual increase of CV cycles, the intensity of Ni<sup>2+</sup>/Ni<sup>3+</sup> redox peak increases and then stabilizes. The increase of the Ni redox peak area is related to the formation of new active species on the catalyst surface [29]. Compared with Re100-NiCr LDH and Re100-S<sub>0.05</sub>-NiCr LDH, Re100-S<sub>0.02</sub>-NiCr LDH exhibits the smallest onset potential of the nickel oxidation peak and the most negative shift of the Ni cathode peak ( $\Delta E_p$ , c = -298 mV). The result shows that appropriate sulfur doping can form active species at lower potentials (Fig. S5a-c) [30]. Obviously, Re100-S<sub>0.02</sub>-NiCr LDH has more uniform CV curve and the highest current density compared to Re100-NiCr LDH and Re100-S<sub>0.05</sub>-NiCr LDH, which can be attributed to the proper sulfur doping optimize the reconfiguration process of NiCr

LDH (Fig. S5d).

The catalytic performance of different catalysts after 100 CV cycles was investigated. The linear scanning voltammetry (LSV) curves show that the overpotentials of Re100-NiCr LDH, Re100-S<sub>0.02</sub>-NiCr LDH, Re100-S<sub>0.05</sub>-NiCr LDH, RuO<sub>2</sub>, and NF are 285.4, 244.4, 336.4, 408.4, and 535.4 mV at 100 mA cm<sup>-2</sup>, respectively (Fig. 2a, b). The Tafel slope plots indicate that Re100-S<sub>0.02</sub>-NiCr LDH has the lowest Tafel slope among these samples, revealing fast OER kinetics (Fig. 2c). Moreover, Re100-S<sub>0.02</sub>-NiCr LDH displays the lowest overpotential and Tafel slope compared to the reported OER catalysts (Fig. 2d, Table S2). The double-layer capacitance ( $C_{dl}$ ) is calculated from the CV curve (Fig. S6). Re100-S<sub>0.02</sub>-NiCr LDH displays the highest  $C_{dl}$  (7.87 mF cm<sup>-2</sup>) among all the samples (Fig. 2e) [31]. The roughness factor (RF) and electrochemical surface area (ECSA) values of the catalysts are calculated based on the  $C_{dl}$  values, and the ECSA-normalized LSV curve is shown in Fig. S7. Re100-S<sub>0.02</sub>-NiCr LDH not only has the highest RF and ECSA values among all the samples, but also has the highest performance in the ECSA-normalized LSV curves, suggesting that proper sulfur doping can increase the number of active sites [32,33]. Electrochemical impedance spectroscopy (EIS) was employed to assess the charge transfer rate. Re100-S<sub>0.02</sub>-NiCr LDH demonstrates the smallest charge transfer impedance ( $R_{ct}$ ) among these samples, indicating rapid charge transfer to facilitate OER reaction kinetics (Fig. 2f, Table S3). The electrochemical performance results tentatively suggest that proper sulfur doping can optimize the reconfiguration process of NiCr LDH and accelerate the reaction kinetics. The Cr content before and after 100 CV cycles was measured by inductively coupled plasma atomic emission spectrometer (ICP-AES), as shown in Table S4. After 100 CV cycles, the Cr element is not detected in Re100-S<sub>0.02</sub>-NiCr LDH, indicating complete leaching of Cr. S<sub>0.02</sub>-Ni(OH)<sub>2</sub> is used as pre-catalyst for 100 CV cycles to obtain Re100-S<sub>0.02</sub>-Ni(OH)<sub>2</sub>. The CV and LSV curve are shown in Fig. S8. As the number of CV cycles increases, the current densities of Re100-S<sub>0.02</sub>-NiCr LDH and Re100-S<sub>0.02</sub>-Ni(OH)<sub>2</sub> increase and then level off. The current densities of Re100-S<sub>0.02</sub>-NiCr LDH are higher than those of Re100-S<sub>0.02</sub>-Ni(OH)<sub>2</sub>, indicating that Re100-S<sub>0.02</sub>-NiCr LDH has better



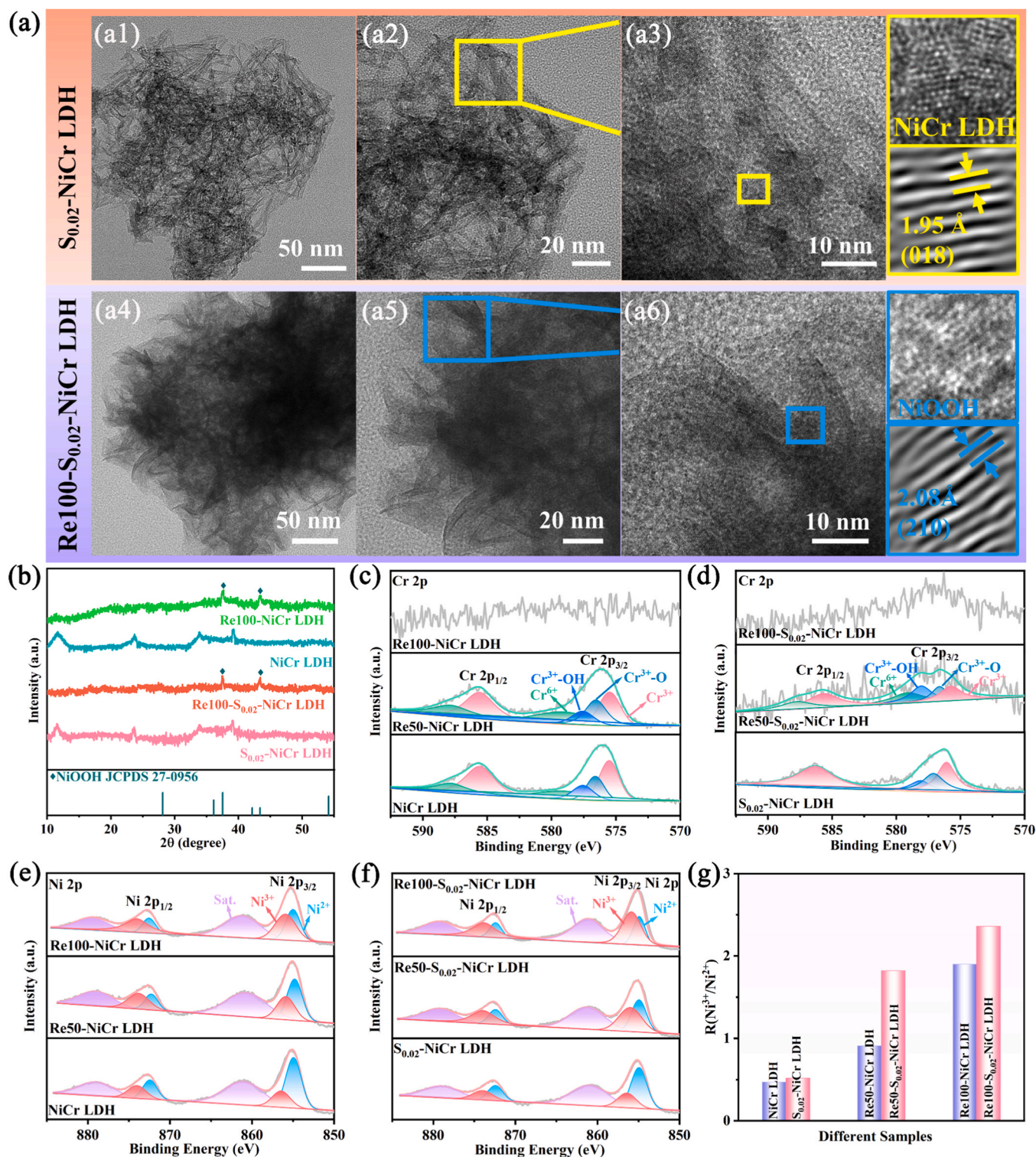


**Fig. 3.** (a) TEM images of  $S_{0.02}$ -NiCr LDH and Re100- $S_{0.02}$ -NiCr LDH. Characterization of ReC-NiCr LDH (C=0, 50 and 100) and ReC- $S_{0.02}$ -NiCr LDH (C=0, 50 and 100): (b) XRD patterns. (c, d) Cr 2p XPS spectra, (e, f) Ni 2p XPS spectra, and (g) the ratio of  $Ni^{3+}$  to  $Ni^{2+}$ .

reconfiguration behavior (Fig. S8a, b). Moreover, the overpotential of Re100- $S_{0.02}$ -NiCr LDH (244.4 mV) is lower than that of Re100- $S_{0.02}$ -Ni(OH)<sub>2</sub> (285.4 mV) at 100 mA cm<sup>-2</sup> (Fig. S8c). The higher OER performance of Re100- $S_{0.02}$ -NiCr LDH is attributed to the fact that Cr leaching promotes the reconfiguration of  $S_{0.02}$ -NiCr LDH and exposed the active site [20].

The surface reconfiguration of catalyst was investigated by different CV cycles. The different CV curves of ReC-NiCr LDH (C=25, 50 and 100)

and ReC- $S_{0.02}$ -NiCr LDH (C=25, 50 and 100) show that the current density increases drastically and then levels off as the number of CV cycles increases, suggesting that the catalyst surface undergoes reconfiguration (Fig. S9a-f). Compared to ReC-NiCr LDH (C=25, 50 and 100), all CV curves of ReC- $S_{0.02}$ -NiCr LDH (C=25, 50 and 100) show smoother reconfiguration trend and higher current density, indicating that proper sulfur doping optimizes the surface reconfiguration process (Fig. S9g, h). The metal ion concentration in the electrolyte after different CV is tested



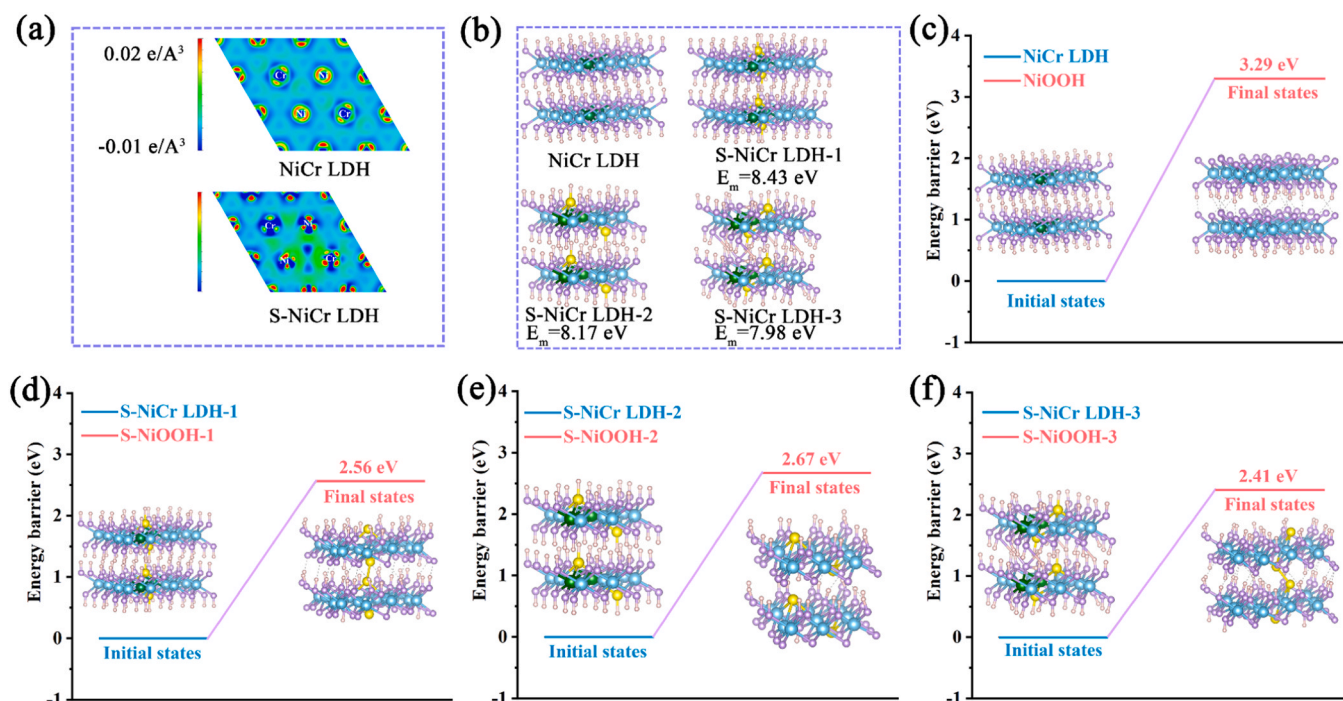


**Fig. 4.** (a) The electron localization function of NiCr LDH and S-NiCr LDH. (b) Structural modeling and corresponding formation energies for NiCr LDH and three sulfur doped different sites. Reconfiguration energy barriers for (c) NiOOH, (d) S-NiOOH-1, (e) S-NiOOH-2, and (f) S-NiOOH-3.

by ICP-AES to investigate the catalyst surface reconfiguration behavior. The Cr leaching concentration increases as the CV cycles increase. The Cr leaching concentrations of ReC-S<sub>0.02</sub>-NiCr LDH (C=25 and 50) are higher than those of ReC-NiCr LDH (C=25 and 50), but the Cr leaching concentration of Re100-S<sub>0.02</sub>-NiCr LDH is lower than that of Re100-NiCr LDH. The results show that proper sulfur doping accelerates the Cr leaching rate and reaches the optimum value of Cr leaching concentration at 100 CV cycles, which better induces the surface reconfiguration of the catalyst (Fig. S9i).

The LSV plot shows that the overpotential of Re25-S<sub>0.02</sub>-NiCr LDH, Re50-S<sub>0.02</sub>-NiCr LDH and Re100-S<sub>0.02</sub>-NiCr LDH decreases from 390, 275.4 to 244.4 mV, and the Tafel slope also decreases gradually, indicating that the electrochemical performance is improved during the reconfiguration process (Fig. S10a-c). In addition, compared with Re25-S<sub>0.02</sub>-NiCr LDH and Re50-S<sub>0.02</sub>-NiCr LDH, Re100-S<sub>0.02</sub>-NiCr LDH has the largest  $C_{dl}$  (Fig. S10d, Fig. S11), while  $R_{ct}$  is opposite (Fig. S10e, Table S5), indicating that the active surface area increases and accelerates charge transfer during the surface reconfiguration process. The stability of Re100-S<sub>0.02</sub>-NiCr LDH was evaluated by chronoamperometry. The Re100-S<sub>0.02</sub>-NiCr LDH remains stable for 60 h at 60 mA cm<sup>-2</sup> (Fig. S10f). Therefore, excellent OER performance of Re100-S<sub>0.02</sub>-NiCr LDH originates from the fact that Cr leaching induces surface reconfiguration and sulfur doping further optimizes the reconfiguration behavior.

Understanding the structural evolution and the actual active site is a prerequisite for revealing the reconfiguration mechanism. ReC-NiCr LDH (C=50 and 100) and ReC-S<sub>0.02</sub>-NiCr LDH (C=50 and 100) were characterized to elucidate the structural changes during the reconfiguration process. SEM images show that the morphology of Re50-NiCr LDH and Re100-NiCr LDH without significant change compared with NiCr LDH (Fig. S12a-c). On the contrary, the morphology of Re50-S<sub>0.02</sub>-NiCr LDH and Re100-S<sub>0.02</sub>-NiCr LDH gradually evolved from network to small nanosheets (Fig. S12d-f). The formation of thin nanosheets facilitates electron transport near the catalyst surface [34]. The morphology changes after reconfiguration were further confirmed by comparing the TEM and HRTEM of S<sub>0.02</sub>-NiCr LDH and Re100-S<sub>0.02</sub>-NiCr LDH. The TEM image of S<sub>0.02</sub>-NiCr LDH shows network morphology (Fig. 3a1, a2),

which confirms the SEM results. The lattice stripes in Fig. 3a3 correspond to the (018) crystal surface of NiCr LDH. After 100 CV cycles, the TEM image of Re100-S<sub>0.02</sub>-NiCr LDH shows the morphology of nanosheets with abundant micropores (marked by orange circles) (Fig. 3a4, a5, and Fig. S13a). The formation of micropores on the nanosheets may be due to Cr leaching during electrochemical activation [19]. The lattice stripes in the HRTEM image correspond to the (210) crystal plane of NiOOH (Fig. 3a6). Moreover, the presence of vacancies in the HRTEM images, which is attributed to Cr leaching leading to the formation of cationic vacancies (Fig. S13b). The cationic vacancies in Re100-S<sub>0.02</sub>-NiCr LDH has abundant defects, which is conducive to increasing the number of catalyst active sites [20]. The XRD patterns of Re100-NiCr LDH and Re100-S<sub>0.02</sub>-NiCr LDH show that the characteristic peaks of LDH disappear, and the peaks at 37.5° and 43.4° correspond to the (011) and (210) crystal planes of NiOOH (Fig. 3b), which is consistent with the TEM results.

The Cr 2p peak of Re50-NiCr LDH can be stabilized, but the Cr 2p peak of Re100-NiCr LDH disappears, indicating that complete leaching of Cr (Fig. 3c). Apparently, the noisy Cr 2p peak of Re50-S<sub>0.02</sub>-NiCr LDH is attributed to Cr leaching during electrochemical activation (Fig. 3d). The reason may be that the strength of the Cr-S bond formed after sulfur doping is lower than that of the Cr-O bond, which accelerates the leaching rate of Cr. Moreover, the Cr<sup>6+</sup> is detected in the Cr 2p peak of Re50-S<sub>0.02</sub>-NiCr LDH, which is due to the oxidation of Cr<sup>3+</sup> at high potentials. The Cr 2p peak in Re100-S<sub>0.02</sub>-NiCr LDH is undetectable due to complete leaching of Cr, which is consistent with the ICP-AES results. The Ni 2p spectra of ReC-NiCr LDH (C=50 and 100) and ReC-S<sub>0.02</sub>-NiCr LDH (C=50 and 100) show significant increase in the peak area of Ni<sup>3+</sup> (Fig. 3e, f). The intensity ratio of Ni<sup>3+</sup>/Ni<sup>2+</sup> in ReC-S<sub>0.02</sub>-NiCr LDH (C=50 and 100) is higher than that of ReC-NiCr LDH (C=50 and 100), suggesting that sulfur doping promotes the conversion of Ni<sup>2+</sup> to the higher valence state (Fig. 3g) [35]. The content of lattice oxygen in ReC-NiCr LDH (C=50 and 100) and ReC-S<sub>0.02</sub>-NiCr LDH (C=50 and 100) decreases with the increase of CV cycles, and the content of V<sub>O</sub> increases (Fig. S14, Table S6). This phenomenon is more obviously observed in ReC-S<sub>0.02</sub>-NiCr LDH (C=50 and 100), indicating that sulfur doping promotes lattice oxygen depletion during the electrochemical activation

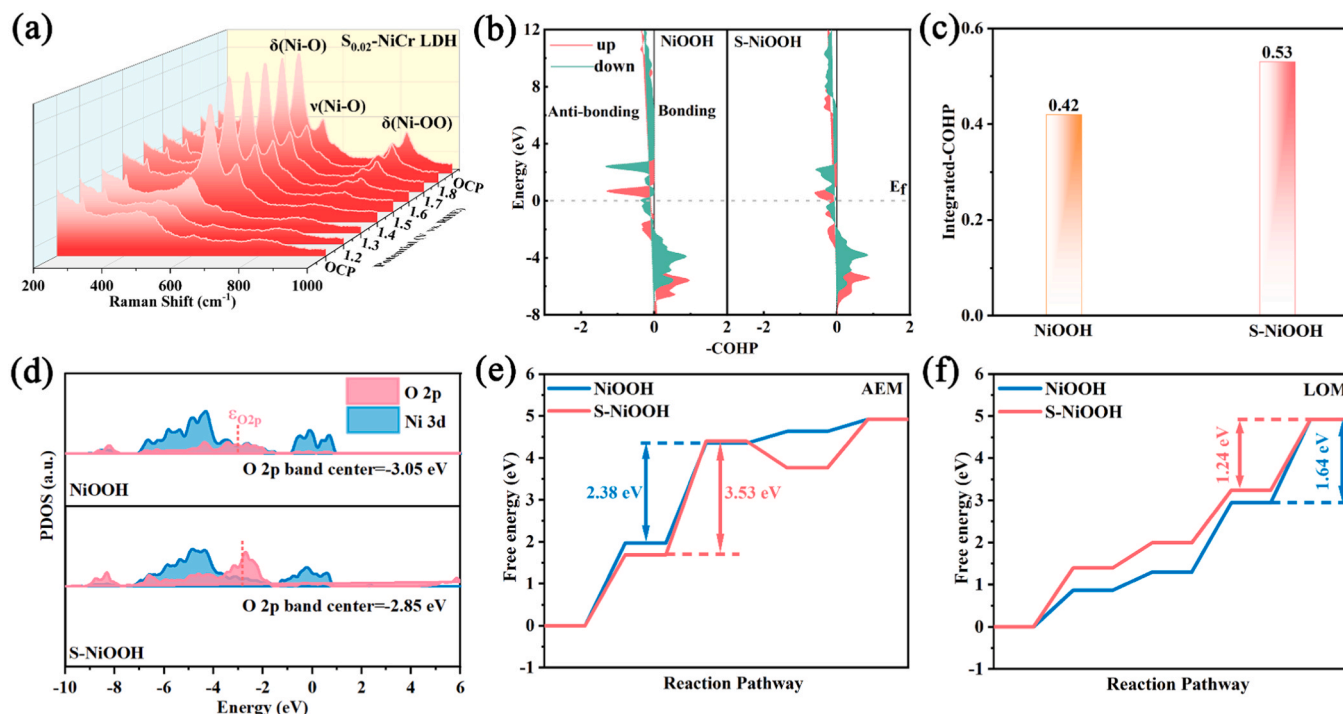


Fig. 5. (a) *In situ* Raman spectra of  $\text{S}_{0.02}\text{-NiCr LDH}$  at different applied potentials. (b) COHP of the Ni-O bond, and (c) the integral-COHP to Fermi level in NiOOH and S-NiOOH. (d) Calculated PDOS of NiOOH and S-NiOOH. (e, f) Gibbs free energy diagrams for NiOOH and S-NiOOH.

process. Combined electrochemical performance and characterization results indicate that sulfur doping promotes Cr leaching and lattice oxygen depletion to form  $\text{V}_\text{O}$ , which facilitates the reconfiguration of NiCr LDH into highly active NiOOH.

The electronic structure of the reconfigured catalyst was further investigated by X-ray absorption near edge structure (XANES) [36]. Fig. S15 shows the normalized Ni K-edge XANES spectra of both catalysts. The absorption threshold of  $\text{Re100-S}_{0.02}\text{-NiCr LDH}$  shift slightly toward higher energy direction in reference to  $\text{S}_{0.02}\text{-NiCr LDH}$ , NiO and Ni foil, suggesting that Ni is oxidized to a higher valence state after reconfiguration, which is consistent with the XPS results [35,37]. The results further confirm that the average oxidation state of Ni increases after reconfiguration, which promotes the reconfiguration of surface  $\text{Ni}^{2+}$  to NiOOH.

The samples after OER stability testing were characterized. The XRD pattern once again confirm the formation of NiOOH (Fig. S16a). The Ni 2p peak shows significant increase in  $\text{Ni}^{3+}$  content after OER stability (Fig. S16b, c). In contrast, Cr 2p peak is undetectable due to Cr leaching in the long-term stability test (Fig. S16d, Table S6). Notably, the content of  $\text{V}_\text{O}$  increases after the OER stability test (Fig. S16e). The S 2p spectra without change (Fig. S16f) [38]. The catalysts after the OER stability test were characterized by SEM and TEM. The SEM and TEM images show that the morphology of  $\text{S}_{0.02}\text{-NiCr LDH}$  evolved from network to nano-sheet after OER stability test (Fig. S17a, b). The lattice fringes correspond to the (111) and (210) crystal planes of NiOOH (Fig. S17c). Therefore, S-NiOOH serves as the active center of OER.

### 2.3. DFT calculation

DFT calculations were applied to reveal the role of sulfur doping on reconfiguration and lattice oxygen oxidation. The electron localization function before and after sulfur doping is shown in Fig. 4a. The blue region around Cr is significantly larger after sulfur doping, which implies the loss of electrons. The simultaneous enlargement of the blue and red regions around Ni comes mainly from the redistribution of the electronic structure due to the introduction of sulfur (blue-red relative

cancellation), with no significant electronic changes. Thus, sulfur doping modulates the electronic structure of NiCr LDH, which confirms the XPS results.

The structural models of three different sulfur doped sites were constructed and the corresponding formation energies were calculated (Fig. 4b) [21]. Experimental results show that Cr leaching induces the reconfiguration of NiCr LDH and S-NiCr LDH into NiOOH and S-NiOOH, and the incorporation of sulfur optimize the reconfiguration behavior. Therefore, the reconfiguration energy barrier of the pre-catalyst was calculated to explain the role of sulfur doping on reconfiguration. The reconfiguration energy barriers of NiOOH, S-NiOOH-1, S-NiOOH-2 and S-NiOOH-3 are 3.29, 2.56, 2.67 and 2.41 eV, respectively, implying that sulfur doping lowers the energy barrier of reconfiguration, thereby promoting the reconfiguration process (Fig. 4c-f). In addition, the bond length of Cr-S is higher than that of Cr-O, which means that the bond energy of Cr-S bond is lower than that of Cr-O bond. As a result, sulfur doping leads to easier leaching of Cr (Fig. S18).

*In situ* Raman spectroscopy was used to detect the dynamic surface reconfiguration of NiCr LDH and  $\text{S}_{0.02}\text{-NiCr LDH}$ . Graphite rods and Hg/HgO electrodes were applied as counter electrodes and reference electrodes, respectively, and NF supported nanosheets were directly used as working electrodes. The Raman signals were recorded at different applied potentials of OCP and 1.2–1.8 V vs. RHE. The peak of NiCr LDH located at  $540.5\text{ cm}^{-1}$  in the interval from OCP to 1.4 V corresponds to  $\text{Ni}^{\text{II}}\text{-O}$  [39]. The peaks at  $473.4$  and  $555.7\text{ cm}^{-1}$  during the voltage interval from 1.5 to 1.8 V correspond to the bending vibration ( $\delta$ ) and stretching vibration ( $\nu$ ) of the Ni-O bond in NiOOH, respectively, which implies the formation of NiOOH [40]. The peak remains unchanged when the voltage returns to the OCP from 1.8 V, indicating an irreversible reconfiguration process (Fig. S19) [41]. *In situ* Raman spectroscopy of  $\text{S}_{0.02}\text{-NiCr LDH}$  shows that the peak at  $475.6\text{ cm}^{-1}$  in the OCP to 1.3 V interval corresponds to the  $\delta(\text{Ni-O})$ . The peak splits into two peaks at  $475.6$  and  $558.1\text{ cm}^{-1}$  in the 1.4–1.8 V interval, and at  $800\text{--}1000\text{ cm}^{-1}$  corresponding to O-O in NiOOH [42,43]. The peak intensity is almost unchanged when the voltage is returned to OCP from 1.8 V, which confirms that the formation of NiOOH is an irreversible



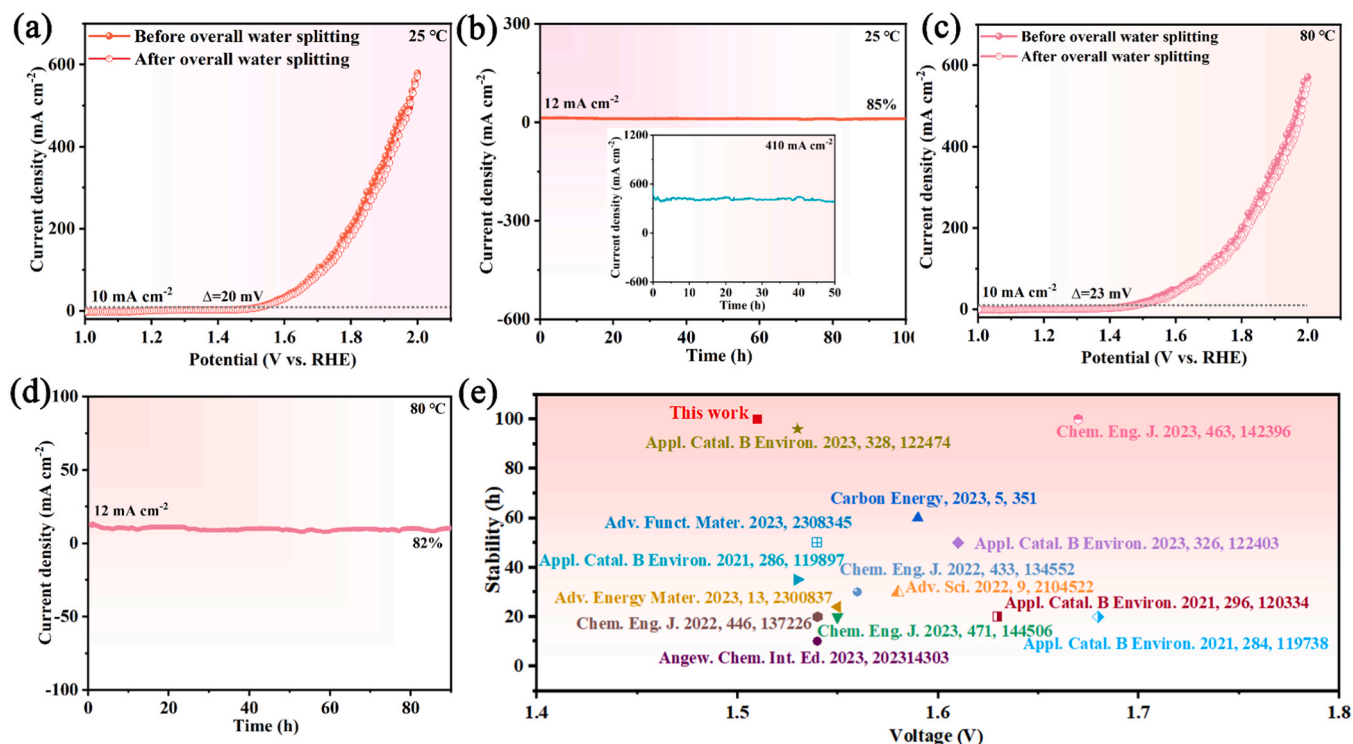


**Fig. 6.** LSV curves before and after stability testing at different temperatures (a) 25 °C, (c) 80 °C, chronoamperometry curves of Re100-S<sub>0.02</sub>-NiCr LDH (b) 25 °C, (d) 80 °C, and (e) comparison of the overall water splitting performance of Re100-S<sub>0.02</sub>-NiCr LDH with the recently reported bifunctional catalysts at 25 °C.

process. Compared to NiCr LDH, S<sub>0.02</sub>-NiCr LDH has a lower oxidation potential for the transition from Ni<sup>2+</sup> to high valent Ni, suggesting that sulfur doping reduces the oxidation potential of Ni<sup>2+</sup> (Fig. 5a).

To elucidate the role of sulfur doping on the OER mechanism, further analysis was performed by DFT calculations. The effect of sulfur doping on the covalency of the Ni-O bond was analyzed by calculating the crystal orbital Hamiltonian pooch (COHP). The negative and positive values of -COHP represent the anti-bonding and bonding states, respectively (Fig. 5b) [44]. The covalent strength of metal-oxygen bonds is quantified by integrating COHP to the Fermi level (IpCOHP) [45]. The larger the absolute value of IpCOHP, the higher the covalency of the metal-oxygen bond [46]. The absolute values of IpCOHP are 0.42 and 0.53 for NiOOH and S-NiOOH, respectively, indicating that the strong covalency of Ni-O in S-NiOOH promotes the involvement of oxygen in the OER via the LOM path (Fig. 5c) [47,48].

The LOM path is characterized by the preferential transfer of electrons from oxygen orbitals rather than metal sites [10]. Therefore, the effect of sulfur doping on the electronic structure of O 2p was further analyzed through partial density of states (PDOS). The position of the O 2p energy band of S-NiOOH is significantly closer to the Fermi level than that of NiOOH, indicating that sulfur doping effectively upshifts the O 2p energy band. From a thermodynamic point of view, the upshift of the O 2p band center causes the O 2p energy level to penetrate deeper into the Fermi level and promotes the outflow of electrons from the oxygen site (Fig. 5d) [49]. Therefore, sulfur doping regulates the energy band structure of lattice oxygen and promotes lattice oxygen oxidation.

The OER activity of the catalysts in the LOM is pH-dependent. To explore the possibility of lattice oxygen involvement, Re100-NiCr LDH and Re100-S<sub>0.02</sub>-NiCr LDH were monitored in KOH electrolytes at different pH values of 12–13.5. The LSV plot shows that OER activity increases with increasing pH (Fig. S20), implying that the LOM is followed. Typically, the activity of AEMs is concentrated on metal sites, involving the generation of \*OH, \*O, and \*OOH intermediates (Fig. S21a) [50,51]. The activated lattice oxygen in the LOM acts as active site [52]. The surface of the catalyst undergoes dynamic changes

during the OER reaction. The activated lattice oxygen accepts OH<sup>-</sup> to form \*OOH species, and O<sub>2</sub> is released to produce Vo, which is refilled by OH<sup>-</sup> (Fig. S21b) [49,53]. Gibbs free energy calculations were performed on the AEM and LOM paths of NiOOH and S-NiOOH to deeply analyze the reaction mechanisms. For AEM, the rate-determining step (RDS) of NiOOH and S-NiOOH is the formation of O\* intermediate, and the corresponding energy barrier is 2.38 and 3.53 eV, respectively (Fig. 5e). The RDS of LOM is the process of OH\* deprotonation, with energy barriers of 1.64 and 1.24 eV, respectively (Fig. 5f). The results show that both NiOOH and S-NiOOH follow the LOM path, and sulfur doping can reduce the energy barrier of RDS [54]. Thus, DFT calculations demonstrate that sulfur doping not only lowers the reconstruction energy barrier, but also enhances the covalency of metal-oxygen and upshift of the O 2p band center to promote lattice oxygen oxidation.

#### 2.4. Overall water splitting performance

Hydrogen evolution reaction (HER) performance was tested in 1 M KOH solution. Compared with the other samples, S<sub>0.02</sub>-NiCr LDH has low overpotential (95.6 mV at 10 mA cm<sup>-2</sup>) (Fig. S22a, b, Fig. S23) and Tafel slope (98.9 mV dec<sup>-1</sup>) (Fig. S22c), indicating that the proper sulfur doped can improve the HER performance of the catalyst. The HER reaction of S<sub>0.02</sub>-NiCr LDH follows the Volmer-Heyrovsky mechanism [55–57]. The HER stability of S<sub>0.02</sub>-NiCr LDH was tested at the current density of 20 mA cm<sup>-2</sup>, as shown in Fig. S22d. The chronoamperometry curve shows that S<sub>0.02</sub>-NiCr LDH can work continuously for 50 h, and the current has not changed significantly, indicating that the catalyst has good stability. After HER stability testing, the physical phase and chemical composition of S<sub>0.02</sub>-NiCr LDH were detected by XRD and XPS, as shown in Fig. S24. The physical phase and chemical composition of S<sub>0.02</sub>-NiCr LDH have not changed, indicating that it is the active center of HER and has excellent structural stability.

In addition, Re100-S<sub>0.02</sub>-NiCr LDH was utilized as anode and cathode to assemble a two-electrode system to test overall water splitting at different temperatures. The LSV curve shows that Re100-S<sub>0.02</sub>-NiCr LDH

only requires 1.51 V to reach a current density of  $10 \text{ mA cm}^{-2}$  at  $25^\circ\text{C}$  (Fig. 6a). The Re100-S<sub>0.02</sub>-NiCr LDH can run continuously for 100 h at  $12 \text{ mA cm}^{-2}$  (Fig. 6b). The overpotential of Re100-S<sub>0.02</sub>-NiCr LDH only increases by 20 mV after 100 h (Fig. 6a). Moreover, it can also work for 50 h at  $410 \text{ mA cm}^{-2}$  (the inset in Fig. 6b). As displayed in Fig. 6c, d, it only requires 1.47 V to reach  $10 \text{ mA cm}^{-2}$  and maintains stability for 90 h at  $80^\circ\text{C}$ . A more detailed comparison of the decomposition voltage and stability of various catalysts for overall water splitting is presented in Fig. 6e and Table S7, which shows that Re100-S<sub>0.02</sub>-NiCr LDH outperforms previously reported bifunctional catalysts.

### 3. Conclusion

In summary, Cr leaching from S<sub>x</sub>-NiCr LDH pre-catalyst induce surface reconfiguration during OER process. The reconstructed catalyst exhibits low overpotential ( $244.4 \text{ mV}$  at  $100 \text{ mA cm}^{-2}$ ) and high stability ( $60 \text{ h}$  at  $60 \text{ mA cm}^{-2}$ ) for OER. Electrochemical and characterization results reveal that sulfur doping promotes the reconfiguration of NiCr LDH into NiOOH by regulating Cr leaching and reduces the oxidation potential of Ni<sup>2+</sup>. DFT calculations further verified that sulfur doping reduces the bond energy of Cr-S and the reconfiguration energy barrier of NiCr LDH, thus promoting the reconfiguration process. Moreover, sulfur doping lowers the reaction energy barrier of the LOM path, increases the covalency of Ni-O, and enhances the lattice oxygen activity. Therefore, sulfur doping successfully promote surface reconstruction and lattice oxygen oxidation by regulates Cr leaching. The reconfigured catalyst requires a low voltage of 1.51 and 1.47 V to drive a current density of  $10 \text{ mA cm}^{-2}$  for overall water splitting at  $25^\circ\text{C}$  and  $80^\circ\text{C}$ , respectively. This work provides new methods for designing LOM-based catalysts and has profound insights into understanding reconfiguration and reaction mechanism.

### CRedit authorship contribution statement

**Qiaohong Su:** Writing-review & editing, Writing-original draft, Validation, Methodology, Investigation, Formal analysis, Data curation, Conceptualization. **Pengyue Wang:** Writing-review & editing, Methodology, Data curation. **Qingcui Liu:** Writing- review & editing. **Rui Sheng:** Writing-review & editing. **Wenhua Cheng:** Writing- review & editing. **Juan Ding:** Writing-review & editing. **Yongpeng Lei:** Writing-review & editing. **Yudai Huang:** Writing-review & editing, Resources, Funding acquisition, Supervisor.

### Declaration of Competing Interest

The authors declare that they have no known competing financial interests or personal relationships that could affect the work reported in this paper.

### Data availability

Data will be made available on request.

### Acknowledgements

This work is financially supported by the National Natural Science Foundation of China (52162036, and 22378342), the Key Project of Nature Science Foundation of Xinjiang Province (2021D01D08), the Major Projects of Xinjiang Province (2022A01005-4 and 2021A01001-1), the Key Research and Development Project of Xinjiang Province (2023B01025-1). Shenzhen Huasuan Technology Co., Ltd. is acknowledged for their contribution to density functional theory (DFT) analysis.

### Appendix A. Supporting information

Supplementary data associated with this article can be found in the

online version at doi:10.1016/j.apcatb.2024.123994.

### References

- [1] N.T. Suen, S.F. Hung, Q. Quan, N. Zhang, Y.J. Xu, H.M. Chen, Electrocatalysis for the oxygen evolution reaction: recent development and future perspectives, *Chem. Soc. Rev.* 46 (2017) 337–365.
- [2] J. Zhou, L. Zhang, Y.C. Huang, C.L. Dong, H.J. Lin, C.T. Chen, L. Tjeng, Z. Hu, Voltage- and time-dependent valence state transition in cobalt oxide catalysts during the oxygen evolution reaction, *Nat. Commun.* 11 (2020) 1984.
- [3] H. Zheng, S. Wang, S. Liu, J. Wu, J. Guan, Q. Li, Y. Wang, Y. Tao, S. Hu, Y. Bai, J. Wang, X. Xiong, Y. Xiong, Y. Lei, The heterointerface between FeI/NC and selenide boosts reversible oxygen electrocatalysis, *Adv. Funct. Mater.* 33 (2023) 2300815.
- [4] J. Song, C. Wei, Z.F. Huang, C. Liu, L. Zeng, X. Wang, Z.J. Xu, A review on fundamentals for designing oxygen evolution electrocatalysts, *Chem. Soc. Rev.* 49 (2020) 2196–2214.
- [5] N. Zhang, Y. Chai, Lattice oxygen redox chemistry in solid-state electrocatalysts for water oxidation, *Energy Environ. Sci.* 14 (2021) 4647–4671.
- [6] I.C. Man, H.Y. Su, F. Calle-Vallejo, H.A. Hansen, J.I. Martínez, N.G. Inoglu, J. Kitchin, T.F. Jaramillo, J.K. Nørskov, J. Rossmeisl, Universality in oxygen evolution electrocatalysis on oxide surfaces, *ChemCatChem* 3 (2011) 1159–1165.
- [7] J. Rossmeisl, Z.W. Qu, H. Zhu, G.J. Kroes, J.K. Nørskov, Electrolysis of water on oxide surfaces, *J. Electroanal. Chem.* 607 (2007) 83–89.
- [8] Z.F. Huang, J. Song, Y. Du, S. Xi, S. Dou, J.M.V. Nsanzimana, C. Wang, Z.J. Xu, X. Wang, Chemical and structural origin of lattice oxygen oxidation in Co-Zn oxyhydroxide oxygen evolution electrocatalysts, *Nat. Energy* 4 (2019) 329–338.
- [9] H. Zhang, Y. Gao, H. Xu, D. Guan, Z. Hu, C. Jing, Y. Sha, Y. Gu, Y.C. Huang, Y. C. Chang, Combined corner-sharing and edge-sharing networks in hybrid nanocomposite with unusual lattice-oxygen activation for efficient water oxidation, *Adv. Funct. Mater.* 32 (2022) 2207618.
- [10] X. Wang, H. Zhong, S. Xi, W.S.V. Lee, J. Xue, Understanding of oxygen redox in the oxygen evolution reaction, *Adv. Mater.* 34 (2022) 2107956.
- [11] Z. Shi, Y. Wang, J. Li, X. Wang, Y. Wang, Y. Li, W. Xu, Z. Jiang, C. Liu, W. Xing, Confined Ir single sites with triggered lattice oxygen redox: toward boosted and sustained water oxidation catalysis, *Joule* 5 (2021) 2164–2176.
- [12] H.J. Liu, S. Zhang, W.Y. Yang, N. Yu, C.Y. Liu, Y.M. Chai, B. Dong, Directional reconstruction of iron oxides to active sites for superior water oxidation, *Adv. Funct. Mater.* 33 (2023) 2303776.
- [13] A. Wang, W. Wang, J. Xu, A. Zhu, C. Zhao, M. Yu, G. Shi, J. Yan, S. Sun, W. Wang, Enhancing oxygen evolution reaction by simultaneously triggering metal and lattice oxygen redox pair in iridium loading on Ni-doped Co<sub>3</sub>O<sub>4</sub>, *Adv. Energy Mater.* 13 (2023) 2302537.
- [14] P.P. Lopes, D.Y. Chung, X. Rui, H. Zheng, H. He, P. Farinazzo Bergamo Dias Martins, D. Strmcnik, V.R. Stamenkovic, P. Zapol, J. Mitchell, Dynamically stable active sites from surface evolution of perovskite materials during the oxygen evolution reaction, *J. Am. Chem. Soc.* 143 (2021) 2741–2750.
- [15] Y. Sun, J. Wu, Y. Xie, X. Wang, K. Ma, Z. Tian, Z. Zhang, Q. Liao, W. Zheng, Z. Kang, Dynamics of both active phase and catalysis pathway for spinel water-oxidation catalysts, *Adv. Funct. Mater.* 32 (2022) 2207116.
- [16] D. Xu, S. Liu, M. Zhang, L. Xu, H. Gao, J. Yao, Manipulating the dynamic self-reconstruction of CoP electrocatalyst driven by charge transport and ion leaching, *Small* 19 (2023) 2300201.
- [17] Y. Zhao, Q. Wen, D. Huang, C. Jiao, Y. Liu, Y. Liu, J. Fang, M. Sun, L. Yu, Operando reconstruction toward dual-cation-defects Co-containing NiFe oxyhydroxide for ultralow energy consumption industrial water splitting electrolyzer, *Adv. Energy Mater.* 13 (2023) 2203595.
- [18] H. Guo, L. Zhang, D. Ou, Q. Liu, Z. Wu, W. Yang, Z. Fang, Q. Shi, Zn-leaching induced rapid self-reconstruction of NiFe-layered double hydroxides for boosted oxygen evolution reaction, *Small* (2023) 2307069.
- [19] A. Malek, Y. Xue, X. Lu, Dynamically restructuring Ni<sub>x</sub>Cr<sub>y</sub>O electrocatalyst for stable oxygen evolution reaction in real seawater, *Angew. Chem. Int. Ed.* 135 (2023) e202309854.
- [20] Y. Duan, J.Y. Lee, S. Xi, Y. Sun, J. Ge, S.J.H. Ong, Y. Chen, S. Dou, F. Meng, C. Diao, Anodic oxidation enabled cation leaching for promoting surface reconstruction in water oxidation, *Angew. Chem. Int. Ed.* 60 (2021) 7418–7425.
- [21] H. Lei, L. Ma, Q. Wan, S. Tan, B. Yang, Z. Wang, W. Mai, H.J. Fan, Promoting surface reconstruction of NiFe layered double hydroxide for enhanced oxygen evolution, *Adv. Energy Mater.* 12 (2022) 2202522.
- [22] W. Chen, B. Wu, Y. Wang, W. Zhou, Y. Li, T. Liu, C. Xie, L. Xu, S. Du, M. Song, Deciphering the alternating synergy between interlayer Pt single-atom and NiFe layered double hydroxide for overall water splitting, *Energy Environ. Sci.* 14 (2021) 6428–6440.
- [23] Y. Yang, L. Dang, M.J. Shearer, H. Sheng, W. Li, J. Chen, P. Xiao, Y. Zhang, R. J. Hamers, S. Jin, Highly active trimetallic NiFeCr layered double hydroxide electrocatalysts for oxygen evolution reaction, *Adv. Energy Mater.* 8 (2018) 1703189.
- [24] Q. Su, Q. Liu, P. Wang, J. Ding, W. Cheng, Y. Huang, Fe doping regulates the surface reconstruction and activates lattice oxygen of NiCr LDH for water oxidation, *Chem. Eng. J.* 483 (2024) 149383.
- [25] R. Chen, Z. Zhang, Z. Wang, W. Wu, S. Du, W. Zhu, H. Lv, N. Cheng, Constructing air-stable and reconstruction-inhibited transition metal sulfide catalysts via tailoring electron-deficient distribution for water oxidation, *ACS Catal.* 12 (2022) 13234–13246.



- [26] B. Dasgupta, J.N. Hausmann, R. Beltrán-Suito, S. Kalra, K. Laun, I. Zebger, M. Driess, P.W. Menezes, A facile molecular approach to amorphous nickel pnictides and their reconstruction to crystalline potassium-intercalated  $\gamma$ -NiOOH, enabling high-performance electrocatalytic water oxidation and selective oxidation of 5-hydroxymethylfurfural, *Small* 19 (2023) 2301258.
- [27] M. Liu, Y. Wang, T. Yu, L. Zhan, X. Zhao, C. Lian, Y. Xiong, X. Xiong, Y. Lei, One-step synthesized  $\text{Bi}_5\text{O}_7\text{I}$  for extremely low-temperature  $\text{CO}_2$  electroreduction, *Sci. Bull.* 68 (2023) 1238–1242.
- [28] L. Zhuang, Y. Jia, H. Liu, Z. Li, M. Li, L. Zhang, X. Wang, D. Yang, Z. Zhu, X. Yao, Sulfur-modified oxygen vacancies in iron-cobalt oxide nanosheets: enabling extremely high activity of the oxygen evolution reaction to achieve the industrial water splitting benchmark, *Angew. Chem. Int. Ed.* 59 (2020) 14664–14670.
- [29] Y. Li, Y. Wu, H. Hao, M. Yuan, Z. Lv, L. Xu, B. Wei, In situ unraveling surface reconstruction of  $\text{Ni}_5\text{P}_4/\text{FeP}$  nanosheet array for superior alkaline oxygen evolution reaction, *Appl. Catal. B: Environ. Energy* 305 (2022) 121033.
- [30] S. Li, Z. Li, R. Ma, C. Gao, L. Liu, L. Hu, J. Zhu, T. Sun, Y. Tang, D. Liu, A glass-ceramic with accelerated surface reconstruction toward the efficient oxygen evolution reaction, *Angew. Chem. Int. Ed.* 133 (2021) 3817–3824.
- [31] H.J. Liu, S. Zhang, W.Y. Yang, N. Yu, C.Y. Liu, Y.M. Chai, B. Dong, Directional reconstruction of iron oxides to active sites for superior water oxidation, *Adv. Funct. Mater.* 33 (2023) 2303776.
- [32] D. Chen, H. Bai, J. Zhu, C. Wu, H. Zhao, D. Wu, J. Jiao, P. Ji, S. Mu, Multiscale hierarchical structured NiCoP enabling ampere-level water splitting for multi-scenarios green energy-to-hydrogen systems, *Adv. Energy Mater.* 13 (2023) 2300499.
- [33] J. Lin, H. Zhou, R. Amin, A.E. Fetohi, K. El-Khatib, C. Wang, L. Guo, Y. Wang, In situ formation of nickel sulfide quantum dots embedded into a two-dimensional metal-organic framework for water splitting, *Inorg. Chem. Front.* 10 (2023) 1294–1304.
- [34] J. Duan, Y. Li, Y. Pan, N. Behera, W. Jin, Metal-organic framework nanosheets: an emerging family of multifunctional 2D materials, *Coord. Chem. Rev.* 395 (2019) 25–45.
- [35] M. Han, N. Wang, B. Zhang, Y. Xia, J. Li, J. Han, K. Yao, C. Gao, C. He, Y. Liu, High-valent nickel promoted by atomically embedded copper for efficient water oxidation, *ACS Catal.* 10 (2020) 9725–9734.
- [36] B. Ravel, M. Newville, Athena, artemis, hephaestus: data analysis for X-ray absorption spectroscopy using IFEFFIT, *J. Synchrotron Radiat.* 12 (2005) 537–541.
- [37] Q. Wang, Q. Feng, Y. Lei, S. Tang, L. Xu, Y. Xiong, G. Fang, Y. Wang, P. Yang, J. Liu, W. Liu, X. Xiong, Quasi-solid-state Zn-air batteries with an atomically dispersed cobalt electrocatalyst and organohydrogel electrolyte, *Nat. Commun.* 13 (2022) 3689.
- [38] B. Zhao, J. Liu, X. Wang, C. Xu, P. Sui, R. Feng, L. Wang, J. Zhang, J.L. Luo, X.Z. Fu,  $\text{CO}_2$ -emission-free electrocatalytic  $\text{CH}_3\text{OH}$  selective upgrading with high productivity at large current densities for energy saved hydrogen co-generation, *Nano Energy* 80 (2021) 105530.
- [39] Y.J. Wu, J. Yang, T.X. Tu, W.Q. Li, P.F. Zhang, Y. Zhou, J.F. Li, J.T. Li, S.G. Sun, Evolution of cationic vacancy defects: a motif for surface restructuring of OER precatalyst, *Angew. Chem. Int. Ed.* 60 (2021) 26829–26836.
- [40] X. Bo, Y. Li, X. Chen, C. Zhao, Operando Raman spectroscopy reveals Cr-induced-phase reconstruction of NiFe and CoFe oxyhydroxides for enhanced electrocatalytic water oxidation, *Chem. Mater.* 32 (2020) 4303–4311.
- [41] J. Huang, Y. Li, Y. Zhang, G. Rao, C. Wu, Y. Hu, X. Wang, R. Lu, Y. Li, J. Xiong, Identification of key reversible intermediates in self-reconstructed nickel-based hybrid electrocatalysts for oxygen evolution, *Angew. Chem. Int. Ed.* 131 (2019) 17619–17625.
- [42] C. Hu, Y. Hu, C. Fan, L. Yang, Y. Zhang, H. Li, W. Xie, Surface-enhanced Raman spectroscopic evidence of key intermediate species and role of NiFe dual-catalytic center in water oxidation, *Angew. Chem. Int. Ed.* 60 (2021) 19774–19778.
- [43] X. Zhang, H. Yi, M. Jin, Q. Lian, Y. Huang, Z. Ai, R. Huang, Z. Zuo, C. Tang, A. Amini, In situ reconstructed Zn doped  $\text{Fe}_x\text{Ni}_{(1-x)}\text{OOH}$  catalyst for efficient and ultrastable oxygen evolution reaction at high current densities, *Small* 18 (2022) 2203710.
- [44] H. Lei, Q. Wan, S. Tan, Z. Wang, W. Mai, Pt-quantum-dot-modified sulfur-doped NiFe layered double hydroxide for high-current-density alkaline water splitting at industrial temperature, *Adv. Mater.* 35 (2023) 2208209.
- [45] C. Jia, X. Xiang, J. Zhang, Z. He, Z. Gong, H. Chen, N. Zhang, X. Wang, S. Zhao, Y. Chen, Shifting oxygen evolution reaction pathway via activating lattice oxygen in layered perovskite oxide, *Adv. Funct. Mater.* 33 (2023) 2301981.
- [46] Y. Li, B. Wei, M. Zhu, J. Chen, Q. Jiang, B. Yang, Y. Hou, L. Lei, Z. Li, R. Zhang, Synergistic effect of atomically dispersed Ni-Zn pair sites for enhanced  $\text{CO}_2$  electroreduction, *Adv. Mater.* 33 (2021) 2102212.
- [47] N. Yabuuchi, M. Nakayama, M. Takeuchi, S. Komaba, Y. Hashimoto, T. Mukai, H. Shiiba, K. Sato, Y. Kobayashi, A. Nakao, Origin of stabilization and destabilization in solid-state redox reaction of oxide ions for lithium-ion batteries, *Nat. Commun.* 7 (2016) 13814.
- [48] J.T. Mefford, X. Rong, A.M. Abakumov, W.G. Hardin, S. Dai, A.M. Kolpak, K. P. Johnston, K.J. Stevenson, Water electrolysis on  $\text{La}_{1-x}\text{Sr}_x\text{CoO}_{3-\delta}$  perovskite electrocatalysts, *Nat. Commun.* 7 (2016) 11053.
- [49] A. Grimaud, O. Diaz-Morales, B. Han, W.T. Hong, Y.L. Lee, L. Giordano, K. A. Stoerzinger, M.T. Koper, Y. Shao-Horn, Activating lattice oxygen redox reactions in metal oxides to catalyze oxygen evolution, *Nat. Chem.* 9 (2017) 457–465.
- [50] X. Liu, S. Jing, C. Ban, K. Wang, Y. Feng, C. Wang, J. Ding, B. Zhang, K. Zhou, L. Gan, Dynamic active sites in NiFe oxyhydroxide upon Au nanoparticles decoration for highly efficient electrochemical water oxidation, *Nano Energy* 98 (2022) 107328.
- [51] Q. Wang, Y. Tan, S. Tang, W. Liu, Y. Zhang, X. Xiong, Y. Lei, Edge-hosted Mn-N<sub>4</sub>-C<sub>12</sub> Site tunes adsorption energy for ultralow-temperature and high-capacity solid-state Zn-air Battery, *ACS Nano* 17 (2023) 9565–9574.
- [52] Q. Liu, Q. Su, W. Cheng, J. Ding, W. Zhang, J. Wang, Y. Wang, X. Wang, Y. Huang, Dual role of Fe boost lattice oxygen oxidation of Mo-based materials from kinetics and thermodynamics, *Appl. Catal. B: Environ. Energy* 340 (2024) 123188.
- [53] K. Xiao, Y. Wang, P. Wu, L. Hou, Z.Q. Liu, Activating lattice oxygen in spinel  $\text{ZnCo}_2\text{O}_4$  through filling oxygen vacancies with fluorine for electrocatalytic oxygen evolution, *Angew. Chem. Int. Ed.* 135 (2023) 202301408.
- [54] Q. Wang, S. Tang, Z. Wang, J. Wu, Y. Bai, Y. Xiong, P. Yang, Y. Wang, Y. Tan, W. Liu, X. Xiong, Y. Lei, Electrolyte tuned robust interface towards fast-charging Zn-air battery with atomic Mo site catalyst, *Adv. Funct. Mater.* 33 (2023) 2307390.
- [55] Q. Su, R. Sheng, Q. Liu, J. Ding, P. Wang, X. Wang, J. Wang, Y. Wang, B. Wang, Y. Huang, Surface reconstruction of  $\text{RuO}_2/\text{Co}_3\text{O}_4$  amorphous-crystalline heterointerface for efficient overall water splitting, *J. Colloid Interface Sci.* 658 (2024) 43–51.
- [56] Q. Su, Q. Liu, P. Wang, J. Ding, J. Wang, Y. Huang,  $\text{CuO}_x/\text{Cu}$  nanorod skeleton supported Ru-doped  $\text{CoO}/\text{NC}$  nanocomposites for overall water splitting, *J. Colloid Interface Sci.* 661 (2024) 175–184.
- [57] W. Zhang, Q. Liu, W. Cheng, W. Wang, J. Ding, Y. Huang, Oxygen vacancies enhanced electrocatalytic water splitting of P-FeMoO<sub>4</sub> initiated via phosphorus doping, *J. Colloid Interface Sci.* 660 (2024) 114–123.